Magnetotransport through magnetic domain patterns in permalloy rectangles

M. Bolte,* M. Steiner, C. Pels, M. Barthelmeß, J. Kruse, U. Merkt, and G. Meier
Institut für Angewandte Physik und Zentrum für Mikrostrukturforschung, Universität Hamburg, Jungiusstrasse 11, 20355 Hamburg, Germany

M. Holz and D. Pfannkuche
Institut für Theoretische Physik, Universität Hamburg, Jungiusstrasse 9, 20355 Hamburg, Germany
(Received 31 May 2005; published 30 December 2005)

We study the influence of multidomain configurations on the magnetoresistance of rectangular permalloy microstructures with various thicknesses. The anisotropic magnetoresistance (AMR) is the dominating resistance contribution in these systems. Reversible and irreversible magnetization reversals lead to complex AMR signals. Appropriate positioning of the voltage probes allows the local detection of the magnetoresistance. Two methods for calculating the local AMR, the uniform-current model and diffusive transport calculations, are described. The latter takes potential differences and inhomogenous current paths into account. By comparing magnetoresistance measurements, micromagnetic simulations, and images of magnetic-force microscopy for various film thicknesses, we can exactly link the transitions between magnetic configurations to changes observed in the magnetoresistance.

DOI: 10.1103/PhysRevB.72.224436 PACS number(s): 75.47.−m, 75.50.Bb, 75.60.Ch, 75.60.Jk

I. INTRODUCTION

Electron transport through ferromagnetic microstructures and nanostructures is a hot issue due to its relevance for magnetic memories.[1,2] At present, a lot of progress in understanding the interaction between itinerant and localized electrons is being made.[3–8] With high current densities, the local magnetization can be controlled by the spin-transfer torque which is most attractive as a direct writing process in magnetic random access memory devices (MRAM).[9] In the regime of low current density, the resistance of a ferromagnetic metal can be probed without deteriorating the local magnetization.[7,8] Low current densities are thus used to read out information. Experiments have been performed to analyze the access memory devices (AMR)[10,11] and the resistance caused by a domain wall.[12–17] For the latter there is an ongoing discussion about its sign and existence. Negative as well as positive domain-wall resistances have been theoretically predicted and experimentally demonstrated. It has also been stated that without impurities the resistance of a domain wall vanishes.[18] A possible reason for the contradictive interpretation of the experimental work might be the presence of a local AMR that dominates the domain wall contribution. Thus a proper description and a detailed understanding of the local AMR is essential. To this aim, micromagnetic simulations have proven to be an important tool.[19–23]

We measure the magnetoresistance of permalloy microstructures with local voltage probes and compare the experimental data with simulations. We use the three-dimensional version of the micromagnetic simulation package OOMMF (Ref. 24) which we extended in order to be able to describe local AMR and inhomogeneous current distributions. Thus it is possible to calculate the magnetoresistance of simulated magnetic configurations and to observe transitions between magnetic states through reversible and irreversible changes. The results are compared with AMR measurements and cross-checked by magnetic-force microscopy (MFM).

II. SAMPLE PREPARATION

We have prepared permalloy rectangles with thicknesses between 10 and 100 nm. The different domain patterns that arise due to the distinct thicknesses and lateral sizes of these rectangles have been described in earlier publications.[21,25,26] Gold contacts for magnetoresistance measurements were added to the 4×2-μm^2-sized rectangles with thicknesses 20, 40, and 70 nm as can be seen in Fig. 1. The voltage probes were prepared to cover a rectangle approximately one-fourth of its width. This way we are able to resolve local magnetic configurations with a mirror symmetry along the long axis (the x direction in Fig. 1). External fields can be applied in-plane under an arbitrary angle φ with respect to the long axis. All transport measurements were performed in a helium cryostat at temperatures between 2 and 50 K.

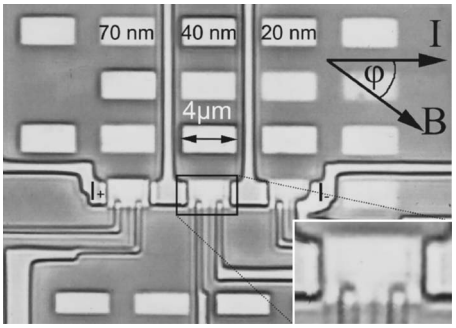

FIG. 1. Array of 4×2 μm^2 permalloy rectangles, three of them contacted. The current contacts are labeled with $\boldsymbol{I}_+$ and $\boldsymbol{I}_-$. The in-plane angle φ between the magnetic field $\boldsymbol{B}$ and the current $\boldsymbol{I}$ is illustrated. The inset shows the 40 nm thick element with its current and voltage probes. The voltage probes are $l=1$ μm apart and reach $w=500$ nm across the sample.

III. MICROMAGNETIC SIMULATIONS

For the simulations, the AMR with its well-known $\cos^2$ dependence between the magnetization and the current,

$$\rho = \rho_\perp + \Delta\rho \cos^2 \theta, \tag{1}$$

is used.[10,27] Here, θ is the angle between the local magnetization and the local current, since the AMR is calculated for every simulation cell and not according to the macrospin model, $\Delta\rho=\rho_\parallel-\rho_\perp$ is the change in resistivity due to the AMR, and $\rho_\perp$ and $\rho_\parallel$ are the resistivities of the thin film when the magnetic field is perpendicular ($\varphi=90°$) and parallel ($\varphi=0°$) to the current direction, respectively. An average value, $\rho_{ave}=(2\rho_\perp+\rho_\parallel)/3$ is defined for the resistivity at remanence for bulk material and $\rho_{ave}=(\rho_\perp+\rho_\parallel)/2$ for extended thin films.[10] The AMR typically adds about 2% to the total resistivity of permalloy.[27,28]

To calculate the domain patterns, the 4×2 μm^2 elements were simulated by applying a finite-difference mesh with a cubic cell size of 10 nm. The material parameters for the simulation are as follows: The anisotropy constant 100 J/m^3, the saturation magnetization 8.6×10^5 A/m, and the exchange constant 1.3×10^{-11} J/m. For the 20-nm-thin rectangles, the simulations were repeated for the *s*-ground state using a conjugate gradient algorithm for the magnetization relaxation and a cell size of 5 nm. The magnetization patterns are virtually unaltered and lead to almost identical AMR curves as the 10 nm cells. The damping coefficient α was set to 0.5 and the precession term of the Landau-Lifshitz equation was turned off to minimize computation time. In quasistatic state transitions such as the present ones, the precession term does not lead to different results since the angle between effective field and magnetization remains small, and the magnetization can move straight towards the direction of the effective field. Also to optimize performance, the conventional Euler evolver as opposed to a more sophisticated Runge-Kutta scheme was used for the present quasistatic problem.[19]

Two different approaches are used to simulate the local AMR. The first one, hereafter called the uniform-current model, assumes that the electric current density is uniform and propagates along the *x* direction through the ferromagnet, thus neglecting the influence of the magnetization and the impact of the low-ohmic gold contacts on the current. The AMR was computed separately for each simulation cell and not simply integrated over the whole sample volume as in the macrospin model. The macrospin model averages out local effects which often leads to wrong results. The voltage calculated between the voltage probes is the sum of all cellwise resistivities multiplied by the incoming current and the ratio l/wt of the distance $l=1$ μm between the voltage probes and the product of the probes' extension across the rectangle $w=500$ nm and the thickness t of the film.

The second approach computes the actual, nonhomogeneous current density by taking the gold contacts and the influence of the AMR on the current into account. This is done by solving the diffusive transport equation,[29] thereby extending the model that has previously been applied for ferromagnetic disks.[30] It generates a finite-element mesh and uses the local magnetization from the micromagnetic simulation. The potential difference between the voltage contacts is computed from the resistivities $\rho_\perp$ and $\rho_\parallel$ by taking into account the geometry of the permalloy and gold structures.

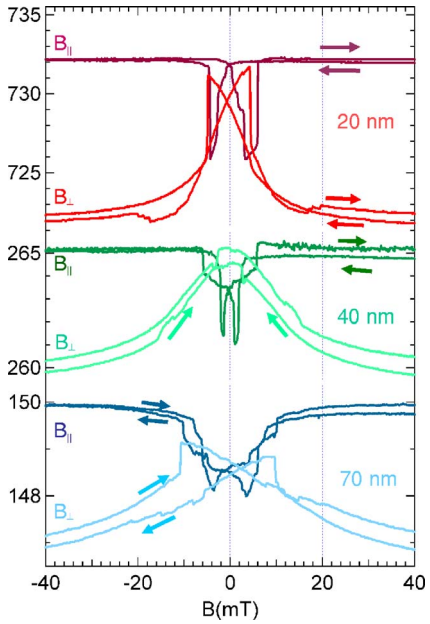

FIG. 2. (Color online) Magnetoresistance measurements of the 20 nm (red), 40 nm (green), and 70 nm (blue) permalloy element at $T=50$ K. The AMR is measured in magnetic fields parallel and perpendicular to the principal direction of the current.

The resistivities of the permalloy were determined by mapping the real geometry of the magnetic structure and its contacts onto a three-dimensional finite-element (FE) mesh. The thicknesses of the permalloy and of the gold (40 nm) were taken into consideration. A current matching the input current of the experiment (50 μA) was placed between the left and right current contacts. By solving the diffusive transport and Poisson's equation, the potential at every node of the FE mesh was derived (see Sec. VII). The resistivity $\rho_\parallel$ was thereby used as a fit parameter to adjust the resulting potential difference at the voltage contacts to the values of the measurements. This yielded a value for $\rho_\parallel$ of 44 $\mu\Omega$ cm. For the resistivity of gold, 2.2 $\mu\Omega$ cm was used.

The AMR ratios $\Delta\rho/\rho_{ave}$ were determined experimentally. The magnetoresistances for angles $\varphi=0°$ and close to 90° are depicted in Fig. 2. The curvature of the AMR signals due to the Lorentz force can be neglected. All curves show irreversible and reversible transitions in the magnetization marked by abrupt and gradual changes in the resistivity, respectively. For 20-, 40-, and 70-nm-thick rectangles, we obtain AMR ratios of 1.4%, 1.9%, and 2.4%, respectively. The highest resistances are observed in saturation for $\varphi=0°$, when the magnetic field is parallel to the current. For decreasing field strengths, the magnetization turns out of the long axis to reduce the stray-field energy and states with magnetization components perpendicular to the *x* direction appears. These states decrease the resistivity. At saturation in transverse geometry, when φ is close to 90° (Ref. 31), all magnetic moments are oriented perpendicular to the current resulting in the lowest possible resistance. In the thicker structures, the

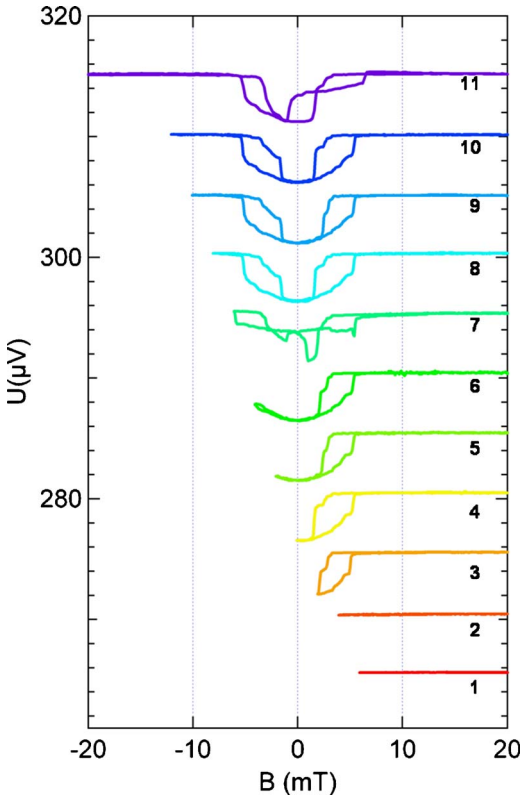

FIG. 3. (Color online) Minor loops of the 40-nm-thick element at $T=2$ K. The traces 2 to 11 are successively shifted upwards by 5 μV.

$\cos^2$ term dominates the irreversible magnetization changes. Also noticeable in Fig. 2 is the different shape of the corresponding curves for different thicknesses. For the thin element, the transitions are abrupt and occur within a narrow field interval. In thicker films vortices can nucleate easier than in thinner films, causing wider field intervals in which the transitions can occur. Because the absolute value of the AMR increases less (from 1.4% to 2.4%) than the interval width (from 7 to 30 mT), the average slopes decrease from 4×10^{-3}/mT to 1.6×10^{-3}/mT. This corresponds to the fact that there are less geometric constraints acting on the magnetization in thicker films so that the vortices can move more easily.[23]

IV. MINOR LOOPS

To understand the interplay between reversible and irreversible magnetization reversals, minor-loop measurements were performed in longitudinal geometry ($\varphi=0°$) for all thicknesses at 2.0 K. In Fig. 3 results are shown for the 40 -nm-thick element. In curves 1 and 2 the magnetoresistance remains virtually constant at fields higher than 4 mT. An irreversible change is recorded in curve 3 between 2 and 5 mT with the typical hysteretic signature. Curves 4 to 6 reveal a subsequent reversible magnetization change. In curve 7, the loop is different from the previous ones, in particular it is asymmetric. In curves 8 to 10, the reversible and irreversible changes occur at the same field strengths and the AMR signals have the same shape. Hence it can be assumed that the sequence of magnetic configurations remains the same. An irreversible change is noted at about −6 mT, so that curves 8 to 10 become symmetric. Finally, curve 11 shows a sweep into saturation and back. Its transition pattern is like the one in curves 8 to 10 for the downward sweep, but different for the upward sweep. The assumed cause for this deviation as well as for the deviation in curve 7 are the different paths the magnetic configuration follows on the energy surface. Impurities such as oxides at the surface can pin the magnetization with an unknown strength. Such pinning on oxide particles was observed on deteriorated samples by MFM. This assumption is investigated further in Sec. VIII with temperature-dependent experiments.

V. UNIFORM-CURRENT MODEL

It has been known for years that only a very limited number of magnetic transitions are possible in soft magnetic rectangles.[32–34] The so-called *c*, *s*, and flower states are the high-remanent ground states for thin permalloy rectangles. The flower state can be disregarded because its total energy is much higher than the ones for the *c* or *s* state.[32,33] In the following, results from micromagnetic simulations are compared to experimental resistances.

In Fig. 4 simulated and measured AMR curves of a 4×2 μm^2 permalloy element with 20 nm thickness are shown in external fields ranging from −20 to 20 mT. The simulations were done according to the uniform-current model with the resistivities determined by diffusive transport calculations (see Sec. III). The geometry of the voltage probes and strength of the current were taken from the experiment. As the actual magnetic configuration in the real sample is unknown and since only the *c* and *s* states exist as high-remanent ground states,[32] these states were used to initialize the simulations. Figures 4(a) and 4(b) refer to the *c* and the *s* state, respectively.

The transitions between magnetization states can be reversible or irreversible. Experimentally, reversible and irreversible transitions are defined from minor loops. For the simulations, the definition is derived from the underlying magnetization states. We consider a transition irreversible when a vortex or a domain wall nucleates or dissolves. Reversible transitions are vortex or domain wall propagations. The measurements were performed at 2.0 K and repeated 20 times for each thickness in positive and negative field direction. Due to temperature and training effects, individual measurements of the same element yield different curves for the first cycles (see Sec. VIII). After about 10 cycles, the AMR curves became stable. Exemplary successive measurements are shown in the lower parts of Figs. 4(a) and 4(b). The step size of the external field for the measurements was 0.1 mT, while the discretization in the simulation was 5 mT between −40 and −10 mT and between 10 and 40 mT, and 1 mT between −10 and 10 mT in Fig. 4(a). For the *s* state, 0.25 mT steps were chosen between 2 and 9 mT.

Figure 4(a) shows two simulated AMR curves for an initial *c* state. To account for mirror-symmetric states, bottom and top contacts at the vertical edges of the boxes enclosed

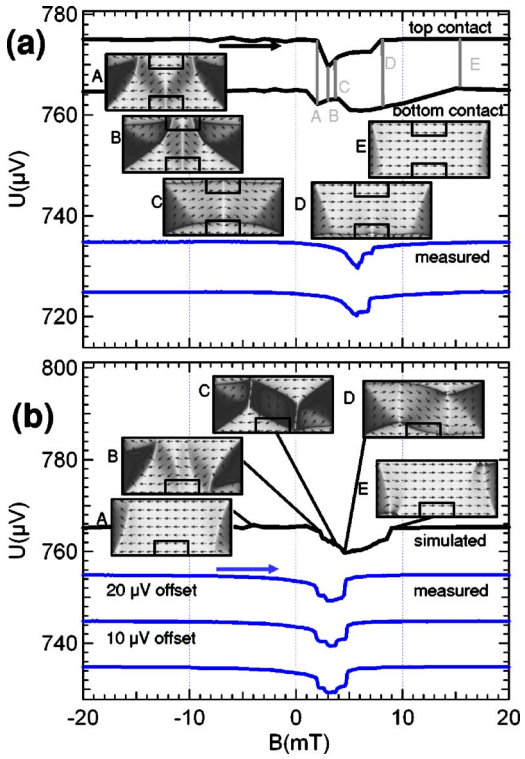

FIG. 4. (Color online) Simulated and experimental traces of the AMR of a 4×2 μm^2 large and 20-nm-thick permalloy structure with two different initial magnetic configurations. (a) Top curves show the simulated AMR for the initial *c*-state, with the upper one offset by +10 μV for clarity. The bottom curves are two corresponding measured AMR signals, the lower one offset by −10 μV. (b) Simulated sweep for the initial *s*-state (top curve) and measurements (bottom) akin to the simulation. Between configurations *A* to *E* irreversible changes occur. The small outlined boxes represent the regions in which the AMR is measured (see voltage probes in Fig. 1) and simulated.

by solid lines were assumed in the calculations. Because of the symmetric positions of the voltage probes with respect to the long edge of the sample, the two possible *s* states yield the same AMR.

When the strength of the external field increases from −40 mT towards zero, the diagonal end domains grow. At a field strength of about 1 mT (state *A*), the domain walls are ε shaped.[35] This causes a noticeable reduction in resistance in the bottom box (bottom curve), while the top region remains uniformly magnetized parallel to the current density. Towards 2 mT (state *B*), the legs of the ε pattern are pushed towards the center of the element. In this situation, the walls enter the top box and a drastic drop in resistance occurs (top curve). The bottom probes notice no major change between states *A* and *B*. For even higher fields (3 mT), the domain between the outer legs of the ε state collapses and the outer domain walls merge into a vortex. This vortex moves towards the bottom edge of the structure until it reaches equilibrium in state *C*. This transition has been previously demonstrated for similar geometries by simulation[35] and x-ray microscopy.[36] It does not result in significant changes in the AMR signal as can be seen in the top two curves of Fig. 4(a) because the average angle of the magnetization with respect to the current density remains basically the same in both regions. In the bottom region, the resistance even increases slightly because the vortex has not entered the bottom box. The unexpected configuration in state *C*, in which a rather thin area is pinned against the edge of a structure, is explained by the torque acting on the magnetic moments due to the strong shape anisotropy at the edges.[35] This torque prevents the magnetic moments from switching into an energetically more favorable direction until the external field is strong enough to overcome the energy barrier between the parallel and the antiparallel configuration. The simulation shows that the domain wall between the pinned domain and the center domain is of a Néel type, with a wall width of about 120 nm. The existence of this narrow edge domain was substantiated by simulations with a smaller cell size (5 nm) and with an external field that was tilted by 0.6° off the long axis. By further increasing the external field, the vortex is moved toward the edge of the sample until, in state *E* (15 mT), the vortex has left the structure and a state close to saturation is reached. This is seen in the bottom contact. The top contact, however, seems to detect a transition into saturation already at point *D*, when the upper domain wall is dissolved. When increasing the thickness of the structure to 40 nm, the domain at the edges dissolves already at about 6 mT.

The measurements in Fig. 4(a) closely correspond to the simulated curve for the top contacts. The same reversible and irreversible resistance changes can be seen, even though the first change, from the initial state over state *A* to *B*, occurs more smoothly in the measurement and at a slightly higher field strength compared to the simulations. An intermediate state *C* and a subsequent jump to a final state *D* can be assumed from the measurements. No further transitions can be seen. Assuming the same underlying transitions in the measurement and in the simulation, we conclude that a *C* state with top-contact arrangement was present in the measurements shown in Fig. 4(a).

In the simulation of Fig. 4(b) which starts with an *s* state at −40 mT, the change of state *A* to *B* appears because a domain wall forms in the sensitive region. From state *B* to *C*, the configuration changes irreversibly by uniting the outer two legs of the *N*-shaped domain pattern into one. The center domain enlarges, while the upper and lower closure domain reduce until at point *D* the 180° walls break apart. At this instance, vortices form at the lower left and upper right ends of the 180° walls. The vortices then move up and down, respectively, through the element to irreversibly form state *D*. This drastic change in magnetization is barely visible in the AMR, because the average angle between local current and magnetization remains almost constant. With increasing field strength, the vortices move towards the upper left and lower right corner of the element, respectively, until the thin Néel walls at the element's upper right and lower left edges collapse. Then the magnetization state is irreversibly transformed into state *E*. The AMR signal does not change any further from that point on because the vortices are well outside the voltage probes. In the measurements, two to three distinct intermediate states can be inferred from the transitions. Even though the measured curves are confined to a smaller field region, the shapes are alike.

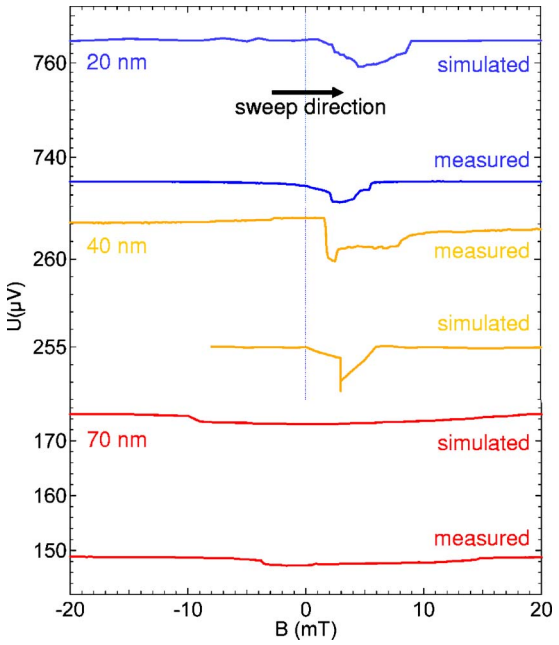

FIG. 5. (Color online) Comparison of measurements at 2 K and simulations for 20-nm- (blue), 40-nm- (yellow), and 70-nm- (red) thick rectangles.

Simulated and measured data for different thicknesses are compared in Fig. 5 in the field range of −20 to 20 mT. The field was applied in the x direction, increasing from −40 to 40 mT. Figure 5 shows good agreement in the absolute values of the AMR as well as in the shapes and locations of the transitions. For the 70 nm-thick rectangles, the magnetization reversal takes place over an extended field interval of about 30 mT, starting with a sharp change in resistance. Changes occur within the same regime for simulation (−10 to 20 mT) and measurement (−6 and 12 mT). For the thinner elements, the transitions are confined to more narrow field ranges. Due to limitations in storage space, the simulations for the 70-nm-thick element were done for a 2×1 μm^2 rectangle. This approach is justified because the magnetization depends more on thickness than on lateral size for elements several microns wide.[20,21,37,38] A more detailed comparison of measurement and simulation follows in Sec. VI.

For the 40-nm-thick element, the measured AMR shows a gradual increase in resistance between −10 and 0 mT, a sharp drop at 2 mT, and a smaller but also sharp increase at 3 mT. The resistance stays almost unchanged up to a field of +8 mT, where the configuration irreversibly changes again and slowly saturates. Two intermediate magnetic states between 2 and 3 mT and between 3 and 8 mT are likely. The simulated transitions are quite similar: between 0 and 3 mT the resistance decreases slowly and at 3 mT it drops sharply. Due to the 1 mT resolution of the simulation, the transition moves from the initial state to the higher intermediate state in one simulation stage as can be seen by the vertical line at 3 mT. The transition shows about the same resistance change as the measurements (0.6 μV). A gradual change from the second intermediate state to the final state is also not seen in the simulation, again due to the limited field resolution. It may also be possible that the vortices in the real sample could not leave the sensitive area between the contacts due to edge roughness[39] or strain caused by the contacts. That would explain the irreversible jump at +8 mT in the experiment. Experiments and simulations for the 20 nm-thin rectangle have already been compared in Fig. 4.

VI. MAGNETIC-FORCE MICROSCOPY

To derive more conclusive information about the magnetization configurations that result in the measured AMR signals, MFM was employed. There is an inherent difficulty to carry out magnetoresistance and MFM measurements simultaneously due to the interaction of the magnetic tip with the sample, which creates a stray field of up to 50 mT.[40,41] Hence, micromagnetic simulations serve as a bridge between AMR and MFM.

In Fig. 6(a), measured (first row) and simulated MFM images (second row) together with their underlying magnetic

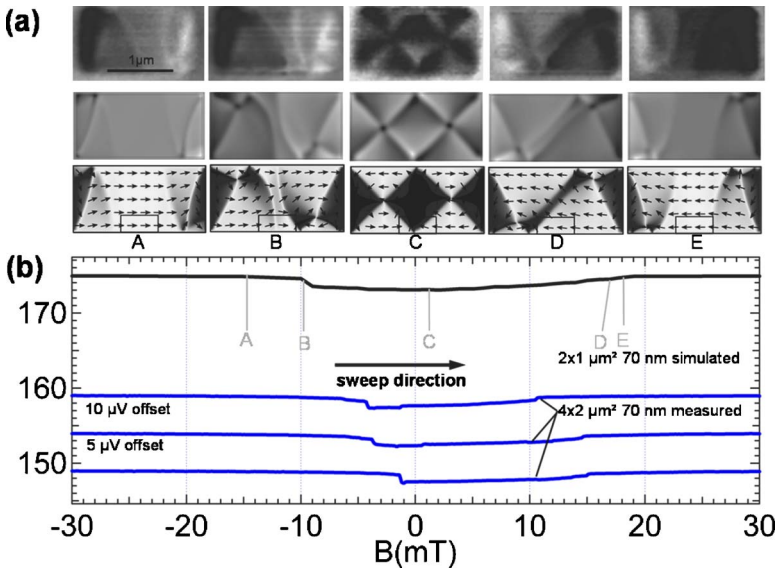

FIG. 6. (Color online) (a) 2×1-μm^2-large and 70-nm-thick permalloy rectangles, measured by MFM (top row). The middle and lower rows show simulated MFM images according to Ref. 26. The gray scale of the lower row ranges from white (magnetization along the long axis) to black (magnetization perpendicular to long axis). (b) Three consecutive AMR measurements (lower curves) performed at 2.0 K on a 4×2-μm^2-large and 70-nm-thick rectangle and an AMR curve simulated for the rectangle in (a).

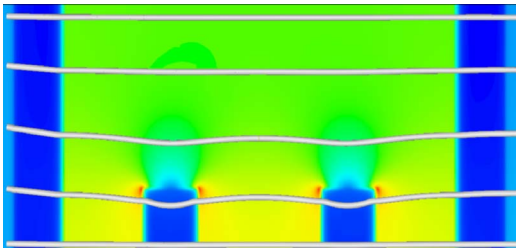

FIG. 7. (Color online) Current distribution just below the surface of the 20-nm-thick permalloy rectangle. The current contacts are attached on the left- and right-hand sides, while the voltage probes lie in the lower part of the figure, on top of the structure. The bright lines illustrate five current paths. Colors represent absolute values of the current density between 0 A/m^2 (blue) and 2.0×10^9 A/m^2 (red).

configurations (third row) are shown for a 2×1 μm^2 large and 70 nm-thick rectangle. Labels *A* to *E* correspond to strengths of the magnetic field as indicated in Fig. 6(b). The calculated MFM images were derived by our OOMMF extension[21,26] according to the algorithm described in Ref. 41. The simulated AMR signal in Fig. 6(b) considers only the region within the black boxes (see also Fig. 4). For comparison, three distinct AMR measurements on a structure with the same lateral aspect ratio and thickness (4×2 μm^2, 70 nm thick) are shown. These measurements show that the transitions observed by MFM coincide almost exactly with the simulated magnetic states (third row) and their MFM images (second row). The simulated magnetizations, in turn, cause the local AMR [Fig. 6(b), top curve]. That AMR curve agrees with the principle shape of the measured signals. The good agreement of measurement and simulation in Fig. 6 demonstrates that the simulated magnetic states *A* to *E* actually occur in real samples and that they lead to AMR signals expected from the geometric positions of the voltage probes in Fig. 1.

VII. DIFFUSIVE TRANSPORT CALCULATIONS

To understand the impact of the low-resistive voltage contacts on the current paths and to calculate the influence of the local AMR more accurately, the conductivities of permalloy and gold, the geometric boundary conditions as well as the local AMR were included in a diffusive transport calculation of the local electric potentials and the current density. The calculations were used first of all to determine the resistivity. For this, the potential difference between the voltage probes was calculated and compared to the measured voltage. The fitting resulted in a resistivity of 44 $\mu\Omega$ cm. The result of such a calculation is shown in Fig. 7. The background color coding reveals a spatial variation of the current density at the top of the permalloy rectangle of about an order of magnitude. It ranges from the permalloy regions right below the highly conductive gold current and voltage contacts (blue, 0 A/m^2 to regions in the permalloy at the corners of the voltage contacts (red, 2.0×10^9 A/m^2.

The calculation of the local current densities and of current paths reveal a noticeable deviation from the uniform-current model. In comparison to the uniform-current model, the current paths change little due to the local AMR, but are largely influenced by the shape and position of the gold contacts. Future work would allow determining the quantitative values of the influences.

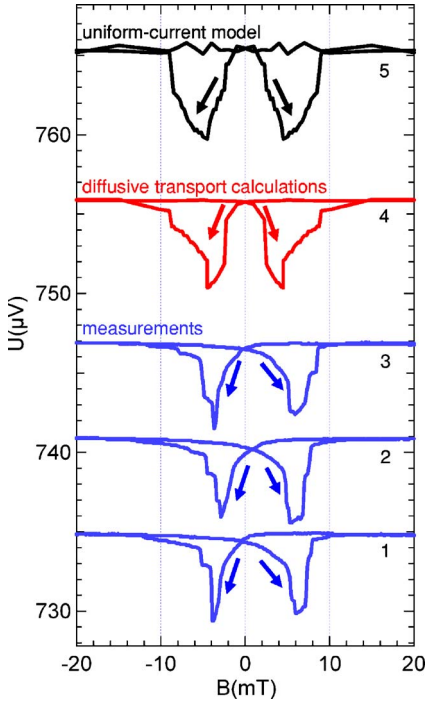

FIG. 8. (Color online) Comparison of the AMR of the two simulation models with experiments: Bottom three curves (blue) are measured AMR signals for the 4×2-μm^2-large and 20-nm-thick permalloy rectangle at 2 K, the top curve (black) shows the results of the uniform-current approach and an initial *s* state, and the middle curve (red) results from the diffusive-transport calculation. Curves 2 to 4 are shifted upwards by 6, 12, and 21 μV.

The potential difference between the voltage contacts was computed for hysteresis loops and yielded results such as the center (red) curve in Fig. 8. The bottom three curves depict measurements. These curves differ in their details due to the low temperature as will be discussed in Sec. VIII. However, the down-sweeps all show two to three irreversible jumps hinting at intermediate magnetic states. The diffusive transport calculation (center curve) shows a similar decrease in resistance with decreasing field strength down to the minimum resistance between −4 and −5 mT, then an increase with two sharp irreversible jumps. The magnetic transitions are more pronounced than for the uniform-current approach (top curve in black). This is even though identical magnetization patterns were used to compute the AMR. The conclusion is that the local AMR is weighed by the absolute value of the current density. In Fig. 7, the corners of the voltage contacts contribute most, so that any resistance changes in these areas, e.g., caused by passing vortices, are amplified in comparison to other regions of the sample.

VIII. TEMPERATURE DEPENDENCE

Temperature-dependent AMR measurements for the 70-nm-thick element are shown in Fig. 9. The hysteretic

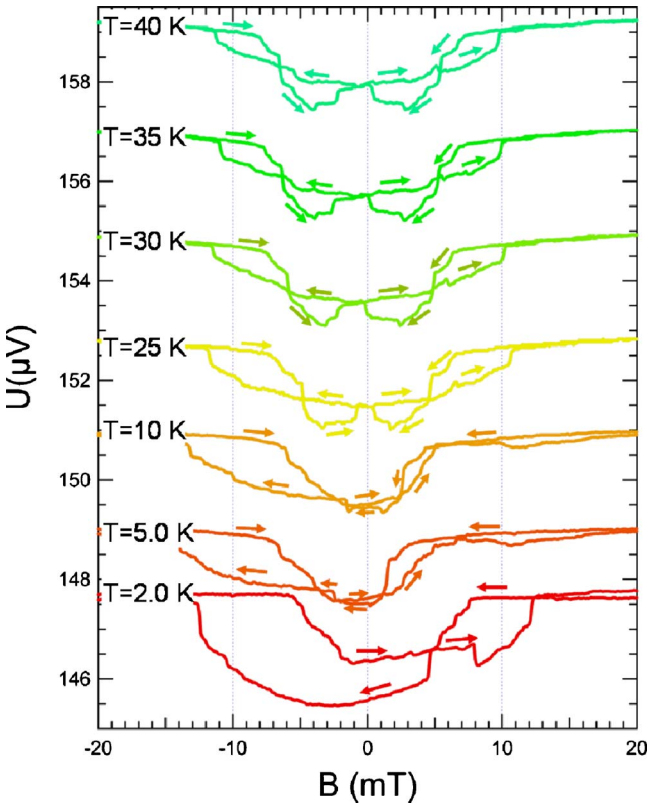

FIG. 9. (Color online) Temperature-dependent AMR measurements of the 70-nm-thick permalloy element. The curves are successively shifted upwards by 2 μV for clarity.

magnetoresistances become more symmetric when the temperature is increased. The transition temperature from asymmetric to symmetric reversals decreases with increasing thickness from about 50 K (20 nm) over 35 K (40 nm) to 25 K (70 nm). This behavior originates from the complex magnetization patterns of the multidomain configurations. The curves will never be completely symmetric, though, due to the random nature of Barkhausen jumps. Samples with simpler magnetic configurations such as nanorings[42–45] do not show a significant temperature-dependence in the AMR curve in the temperature range between 2 to 50 K. This is because the geometrical constrictions in nanorings allow only a very limited number of ground states, namely the onion, the global vortex, and the local vortex state.[45] Such magnetization states are very robust, i.e., they are separated by large energy barriers.

Thermal excitation energies are very small compared to the total energy of the micromagnets. However, the energy differences between different reversal paths can be tiny. This may explain the asymmetry of the magnetoresistance curves for lower temperatures. In the picture of an energy landscape, the system follows local paths for low temperatures. For a flat landscape near equilibrium, a small thermal energy suffices to reach global minima which correspond to symmetric magnetization reversals. In thin films, the energy barriers between distinct magnetic configurations increase. Hence, thin elements show more pronounced irreversible resistance changes and the hysteresis becomes symmetric at higher transition temperatures.

IX. CONCLUSIONS

In conclusion, we have investigated permalloy rectangles with different thicknesses by magnetotransport measurements and compared the results to local AMR simulations. We employed uniform current and diffusive transport calculations. The latter were used to determine the resistivity of the permalloy, the current density, and the current paths through the element. There is good agreement of both calculations with the experiment in respect to the overall value and shape of the AMR signals. However, one must include in the calculations both the presence of the current and voltage contacts and the variation in the local current density to arrive at the absolute values of the resistance and a more precise shape of the hysterectic AMR curves. The reversible and irreversible jumps observed in the measurements can be linked to changes in the magnetic states observed in micromagnetic simulations. The magnetic configurations found in the simulations are supported by MFM. Deviations in the AMR curves are linked to temperature effects. Future investigations would allow the study of interactions between nonuniform currents and the local magnetization with the aid of diffusive-transport calculations in combination with magnetotransport measurements and simulations, e.g., the study of the influence of "hot-spots" in magnetic trilayers[46] or the current flow through nanoconstrictions.

ACKNOWLEDGMENTS

We would like to thank J. Gancarz for his superb technical assistance. Financial support of the Deutsche Forschungsgemeinschaft via the Graduiertenkolleg "Physik nanostrukturierter Festkörper" and the BMBF via the Verbundprojekt 13N8283, via the Sonderforschungsbereich 508 "Quantenmaterialien" and the Sonderforschungsbereich 668 "Magnetismus vom Einzelatom zur Nanostrucktur" is gratefully acknowledged.

*Electronic address: mbolte@physik.uni-hamburg.de

[1] J. C. Slonczewski, J. Magn. Magn. Mater. **159**, L1 (1996).
[2] J. A. Katine, F. J. Albert, R. A. Buhrman, E. B. Myers, and D. C. Ralph, Phys. Rev. Lett. **84**, 3149 (2000).
[3] P. M. Levy and S. Zhang, Phys. Rev. Lett. **79**, 5110 (1997).
[4] G. Tatara and H. Fukuyama, Phys. Rev. Lett. **78**, 3773 (1997).
[5] R. P. van Gorkom, A. Brataas, and G. E. W. Bauer, Phys. Rev. Lett. **83**, 4401 (1999).
[6] S. Zhang and Z. Li, Phys. Rev. Lett. **93**, 127204 (2004).
[7] Z. Li and S. Zhang, Phys. Rev. B **70**, 024417 (2004).
[8] A. Thiaville, Y. Nakatani, J. Miltat, and Y. Suzuki, Europhys. Lett. **69**, 990 (2005).

[9] K. Yagamia, A. A. Tulapurkar, A. Fukushima, and Y. Suzuki, Appl. Phys. Lett. **85**, 5634 (2004); K. Ounadjela (unpublished); M. Kläui, P.-O. Jubert, R. Allenspach, A. Bischof, J. A. C. Bland, G. Faini, U. Rüdiger, C. A. F. Vaz, L. Vila, and C. Vouille, Phys. Rev. Lett. **95**, 026601 (2005).
[10] T. R. McGuire and R. I. Potter, IEEE Trans. Magn. **11**, 1018 (1975).
[11] D. Buntinx, A. Volodin, and C. Van Haesendonck, Phys. Rev. B **70**, 224405 (2004).
[12] U. Rüdiger, J. Yu, S. Zhang, A. D. Kent, and S. S. P. Parkin, Phys. Rev. Lett. **80**, 5639 (1998).
[13] C. Yu, S. F. Lee, J. L. Tsai, E. W. Huang, T. Y. Chen, Y. D. Yao, Y. Liou, and C. R. Chang, J. Appl. Phys. **93**, 8761 (2003).
[14] T. Taniyama, I. Nakatani, T. Namikawa, and Y. Yamazaki, Phys. Rev. Lett. **82**, 2780 (1999).
[15] J. F. Gregg, W. Allen, K. Ounadjela, M. Viret, M. Hehn, S. M. Thompson, and J. M. D. Coey, Phys. Rev. Lett. **77**, 1580 (1996).
[16] U. Ebels, A. Radulescu, Y. Henry, L. Piraux, and K. Ounadjela, Phys. Rev. Lett. **84**, 983 (2000).
[17] R. Danneau, P. Warin, J. P. Attané, I. Petej, C. Beigné, C. Fermon, O. Klein, A. Marty, F. Ott, Y. Samson, and M. Viret, Phys. Rev. Lett. **88**, 157201 (2002); H. Sato, R. Hanada, H. Sugawara, Y. Aoki, T. Ono, H. Miyajima, and T. Shinjo, Phys. Rev. B **61**, 3227 (2000).
[18] V. A. Gopar, D. Weinmann, R. A. Jalabert, and R. L. Stamps, Phys. Rev. B **69**, 014426 (2004).
[19] J. Fidler and T. Schrefl, J. Phys. D **33**, R135 (2000).
[20] R. Hertel and H. Kronmüller, Phys. Rev. B **60**, 7366 (1999).
[21] M. Barthelmeß, C. Pels, A. Thieme, and G. Meier, J. Appl. Phys. **95**, 5641 (2004).
[22] G. Meier, R. Eiselt, M. Bolte, M. Barthelmeß, T. Eimüller, and P. Fischer, Appl. Phys. Lett. **85**, 1193 (2004).
[23] A. Hubert and R. Schäfer, *Magnetic Domains: The Analysis of Magnetic Microstructures* (Springer, Berlin, 1998).
[24] M. Donahue and D. Porter, National Institute of Standards and Technology, Interagency Report No. NISTIR 6376, Gaithersburg, MD, 1999 (unpublished).
[25] C. Pels, M. Barthelmeß, M. Bolte, A. Thieme, and G. Meier, J. Magn. Magn. Mater. **293**, 885 (2005).
[26] M. Barthelmeß, A. Thieme, R. Eiselt, and G. Meier, J. Appl. Phys. **93**, 8400 (2003).
[27] T. G. S. M. Rijks, S. K. J. Lenczowski, R. Coehoorn, and W. J. M. de Jonge, Phys. Rev. B **56**, 362 (1997).
[28] T. G. S. M. Rijks, R. Coehoorn, M. J. H. de Jong, and W. J. M. de Jonge, Phys. Rev. B **51**, 283 (1995).
[29] M. Holz, O. Kronenwerth, and D. Grundler, Phys. Rev. B **67**, 195312 (2003).
[30] P. Vavassori, M. Grimsditch, V. Metlushko, N. Zaluzec, and B. Ilic, Appl. Phys. Lett. **86**, 072507 (2005).
[31] M. Steiner, C. Pels, and G. Meier, J. Appl. Phys. **95**, 6759 (2004).
[32] R. Hertel, Z. Metallkd. **93**, 957 (2002).
[33] W. Rave and A. Hubert, IEEE Trans. Magn. **36**, 3886 (2000).
[34] D. Goll, G. Schütz, and H. Kronmüller, Phys. Rev. B **67**, 094414 (2003).
[35] See Fig. 20 in Ref. 32.
[36] M. Bolte, R. Eiselt, G. Meier, D.-H. Kim, and P. Fischer, J. Appl. Phys. (to be published).
[37] S. Middelhoek, J. Appl. Phys. **34**, 1054 (1963).
[38] T. Trunk, M. Redjdal, A. Kákay, M. F. Ruane, and F. B. Humphrey, J. Appl. Phys. **89**, 7606 (2001).
[39] Y. Nakatani, A. Thiaville, and J. Miltat, Nat. Mater. **2**, 521 (2003).
[40] J. M. García, A. Thiaville, J. Miltat, K. J. Kirk, J. N. Chapman, and F. Alouges, Appl. Phys. Lett. **79**, 656 (2001).
[41] M. Barthelmeß, Ph.D. thesis, University of Hamburg, 2003.
[42] M. Steiner and J. Nitta, Appl. Phys. Lett. **84**, 939 (2004).
[43] M. Steiner, G. Meier, U. Merkt, and J. Nitta, Physica E (Amsterdam) **24**, 124 (2004).
[44] J. Rothman, M. Kläui, L. Lopez-Diaz, C. A. F. Vaz, A. Bleloch, J. A. C. Bland, Z. Cui, and R. Speaks, Phys. Rev. Lett. **86**, 1098 (2001).
[45] M. Kläui, C. A. F. Vaz, L. Lopez-Diaz, and J. A. C. Bland, J. Phys.: Condens. Matter **15**, R985 (2003).
[46] E. R. Nowak, R. D. Merithew, M. B. Weissman, I. Bloom, and S. S. P. Parkin, J. Appl. Phys. **84**, 6195 (1998).